npj | 2D materials and applications

Article

Published in partnership with FCT NOVA with the support of E-MRS

https://doi.org/10.1038/s41699-024-00497-2

Tailoring polarization in WSe_2 quantum emitters through deterministic strain engineering

Athanasios Paralikis, Claudia Piccinini, Abdulmalik A. Madigawa, Pietro Metuh, Luca Vannucci, Niels Gregersen & Battulga Munkhbat

Quantum emitters in transition metal dichalcogenides (TMDs) have recently emerged as a promising platform for generating single photons for optical quantum information processing. In this work, we present an approach for deterministically controlling the polarization of fabricated quantum emitters in a tungsten diselenide (WSe_2) monolayer. We employ novel nanopillar geometries with long and sharp tips to induce a controlled directional strain in the monolayer, and we report on fabricated WSe_2 emitters producing single photons with a high degree of polarization (99 ± 4%) and high purity ($g^{(2)}(0) = 0.030 \pm 0.025$). Our work paves the way for the deterministic integration of TMD-based quantum emitters for future photonic quantum technologies.

Within photonic quantum information technologies, a key component is the source of single photons[1] used to encode the quantum bits. The ideal single-photon source (SPS) should feature deterministic emission of single indistinguishable photons with near-unity collection efficiency and high purity. The spontaneous parametric down-conversion process is a straightforward method[2] for producing highly indistinguishable photons and has been the workhorse of the community for several decades; however, its probabilistic nature results in a significant trade-off between photon purity and efficiency. As an alternative, the two-level system in a semiconductor host material[3] has recently emerged as an attractive platform for the deterministic generation of single photons using the spontaneous emission process. By placing a semiconductor quantum dot (QD) in an optical cavity[4] and by exploiting cavity quantum electrodynamics (cQED) to control the light emission, pure and highly indistinguishable photons have been generated with efficiency as high as ~ 0.6[5,6]. However, the fabrication of high-quality semiconductor QDs requires expensive, complex molecular beam epitaxy growth methods, which represent a significant drawback in developing QD-based sources.

As an alternative, quantum emitters in transition metal dichalcogenides (TMDs) are attractive due to their availability, their ease of integration into nanophotonic structures, and the versatility in engineering their photonic characteristics[7]. While the direct bandgap structure[7,8] of the pristine monolayer form of TMDs allows for an efficient classical light generation, the emission of pure single photons requires additional engineering. The microscopic origin of single-photon emission in TMDs is believed to be from localized excitonic states appearing either due to defects in the crystal lattice or due to the local strain[3,9–13]. Thus, the implementation of single-photon emitters (SPEs) into TMDs has been pursued by using deterministic defect fabrication[12,14,15] as well as by introducing localized strain in TMD monolayers[16,17]. While stress can be applied directly to the flat TMD lattice[10,14,18,19], strain is typically introduced by placing the TMD layer on arrays of nanopillars[12,13,17,20–25] leading to strain concentration at the contact point. The excitonic levels can then be populated either optically[16,26] or electrically[27,28], thus emitting single photons via photo- or electroluminescence, respectively. Incidentally, the properties of interlayer exciton valley pseudospins in TMDs enable spin-orbit locking, and consequently the emission of chiral single photons[29,30], whose orbital angular momentum can carry an additional degree of freedom that can be exploited for quantum information processing.

Similar to QDs, efficient single-photon emission can be obtained from an SPE in a TMD by placing it inside an optical cavity and exploiting cQED. A WSe_2 emitter was recently placed inside an open cavity geometry[26] leading to the demonstration of an efficiency of ~0.65 and an indistinguishability of ~0.02. The cQED effect relies on a matching of polarizations of the dipole of the emitter and the electric field of the optical cavity mode. For the strain-induced SPE, a deformation strain potential—a nanowrinkle, serving as a macroscopic host for the SPE, is produced by the contact of the WSe_2 monolayer with the nanopillar. The polarization of the SPE dipole is then aligned[18,25,31] with the orientation of the wrinkle. Control of the lateral dipole orientation is unnecessary in a rotationally symmetric geometry[26] with two degenerate orthogonally polarized optical cavity modes, where the dipole can couple into either mode. However, the general case requires control of the SPE dipole polarization, and thus the wrinkle orientation, to efficiently

Department of Electrical and Photonics Engineering, Technical University of Denmark, Ørsteds Plads, 2800 Kongens Lyngby, Denmark.
e-mail: bamunk@dtu.dk

couple light into, for example, the polarized TE mode of a planar ridge waveguide as needed for on-chip integrated quantum photonics[32].

In this work, we propose an efficient method for fabricating orientation-controlled nanowrinkles in monolayer WSe_2, and we demonstrate single photon emission with high purity ($g^{(2)}(0) = 0.030 \pm 0.025$) and a high degree of polarization (99 ± 4%). This method consists of transferring flakes onto a nanostructure with long and sharp tips to form one-dimensional (1D) nanowrinkles, thereby controlling the direction of 1D strain and the polarization of the emitted photons. This work paves the way for integrating TMD-based quantum emitters into photonic systems.

Results and discussion

WSe_2 quantum emitters via cylindrical nanopillars

We initially fabricate SPEs by transferring monolayer WSe_2 flakes on an array of conventional[12,21], rotationally symmetric nanopillars. The pillar dimensions were set to ~150 nm in height and 500 nm in diameter. During the transfer, the monolayer adapts to the shape of the pillar due to the application of mechanical strain and is deformed by creating nanowrinkles. The detailed fabrication process is discussed in the "Methods" section and Supplementary Fig. 1 and Supplementary Note 1. In addition to strain engineering, we introduce defects to the monolayer WSe_2 via e-beam irradiation. Such a process is motivated in Supplementary Note 2 and Supplementary Fig. 2. Figure 1a shows a bright-field (BF) image of the fabricated sample with cylindrical pillars, where the WSe_2 monolayer is highlighted with a white outline, and the pillars are identified through their contrast difference, appearing as dark spots. Using a 470 nm light-emitting diode (LED) as an excitation source, we perform photoluminescence (PL, T = 4 K) imaging on the same sample and present it in Fig. 1b. We observe increased photon emission in proximity of a nanopillar (green circle) compared to the emission in the planar region of WSe_2. This PL increase could be attributed to the efficient migration of excitons toward lower-energy states in the strained areas. Interestingly, the brighter PL emission signal seems to be located around the pillar. This suggests that a stronger strain is localized around the pillar, not on top, which is in good agreement with previously reported results[13]. However, the PL image does not clarify how the nanopillar induces local strain in the monolayer.

To provide microscopic details of the deformation around the pillar, we performed scanning electron microscope (SEM) imaging of the fabricated sample, presented in Fig. 1c. The obtained SEM image reveals the formation of four straight nanowrinkles around the pillar. It is generally accepted that these nanowrinkles host quantum emitters due to local strain, and their orientation is what dictates the polarization profile of the emitted single photons from the resulting emitters[18,25,31].

Due to the rotational symmetry of the nanopillar, which applies strain uniformly, the final number and orientation of these nanowrinkles are random, rendering us unable to control these attributes. Moreover, their proximity could affect further optical characterizations, such as purity.

To investigate the impact of closely formed nanowrinkles in the presence of a single pillar on the optical properties of the sample, we measured PL spectra (T = 4 K) from five different spots around the pillar, highlighted with white crosses (S1–S5) and present them in Fig. 1d. A broad emission signal is observed from the planar monolayer region (S1) due to the delocalized exciton and trion states, whereas the collected spectra taken from different spots around the nanowrinkles (S2–S5) exhibit new discrete and narrow emission lines with higher intensities ranging from 730 to 810 nm[21]. These narrow emission lines are attributed to the new localized excitons hosted in the confined systems produced by the strain and defects in the mono- and few-layer WSe_2[7,11,12,14,17,33–35].

Due to the collection area being larger than the emitter region, we partially collect light from the planar monolayer region, resulting in the broad emission being observed in the spectra from the nanowrinkles (S2–S5) ranging between 720–770 nm. This makes isolating individual emission lines associated with potential single-photon emission from the broad multiphoton emission background relatively challenging, even with narrow optical band-pass filters. Moreover, due to the spatial proximity of

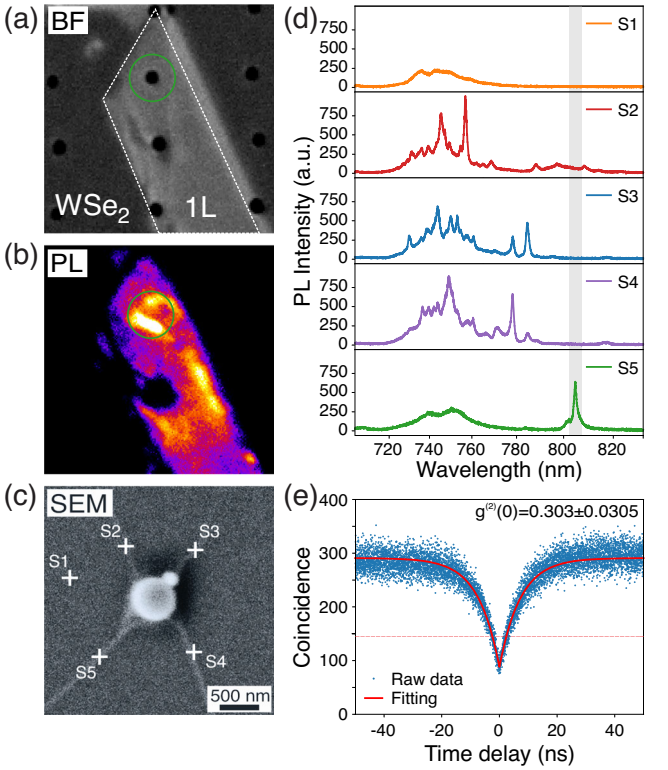

Fig. 1 | WSe_2 quantum emitters with cylindrical pillars. a Bright-field (BF) image of monolayer WSe_2 deposited on cylindrical nanopillars on a Si/SiO_2 substrate. The white outline indicates the WSe_2 monolayer region. **b** Photoluminescence (PL) image of the WSe_2 monolayer flake taken at T = 4 K. The green circle indicates the region around the nanopillar. **c** SEM image of the nanopillar region circled in (**a**) and (**b**), revealing four nanowrinkles that are formed WSe_2 around the pillar. These nanowrinkles are likely to host the potential quantum emitters due to the strain. The crosses indicate the centers of the collection spots for each PL spectra presented in (**d**). **d** PL spectra collected from WSe_2 sample at T = 4 K around the five crosses depicted in (**c**). The obtained PL spectra from S2–5 show narrow emission lines, in contrast to a broad PL emission signal collected from the planar region (S1). **e** Exemplary second-order correlation measurement ($g^{(2)}(\tau)$) of an isolated peak on the presented sample (S5), resulting in $g^{(2)}(0) = 0.303 \pm 0.035$.

the nanowrinkles, the PL spectra exhibit overlapping emission lines as we capture light emitted from multiple emitters simultaneously. These emission lines from different nanowrinkles oriented in the same directions might possess similar polarization profiles (S2–S4, S3–S5), further complicating the process of isolating individual emission lines with polarization filtering. Nevertheless, individual emission lines above 780 nm can be isolated using a long-pass or narrow band-pass optical filter (e.g., S5 in Fig. 1d).

To evaluate the single-photon purity of these emission lines, we performed the second-order autocorrelation ($g^{(2)}(\tau)$) measurement from a representative emission line ($\lambda \approx 807$ nm) under continuous-wave (CW) excitation at 455 nm via a Hanbury Brown–Twiss (HBT) setup. In this setup, the emitted photons are coupled to a 50:50 fiber beam splitter, whose output signals are detected by superconducting nanowire single-photon detectors (SNSPDs). The emission line at 807 nm was spectrally isolated using a 750 nm long-pass filter. Figure 1e shows the obtained correlation histogram, exhibiting a clear signature of photon antibunching. The extracted value of $g^{(2)}(0) = 0.303 \pm 0.035$ is below the $g^{(2)}(0) < 0.5$ threshold, indicating single-photon emission behavior. The reduced purity obtained from the particular emitter can be attributed to emission leakage from nearby SPEs that fall within the diffraction limit of our collection spot. This could be overcome by spatially isolating the nanowrinkles via novel nanostructure designs and subsequently controlling their directionality. The challenges posed by the lack of control of the localization and polarization in

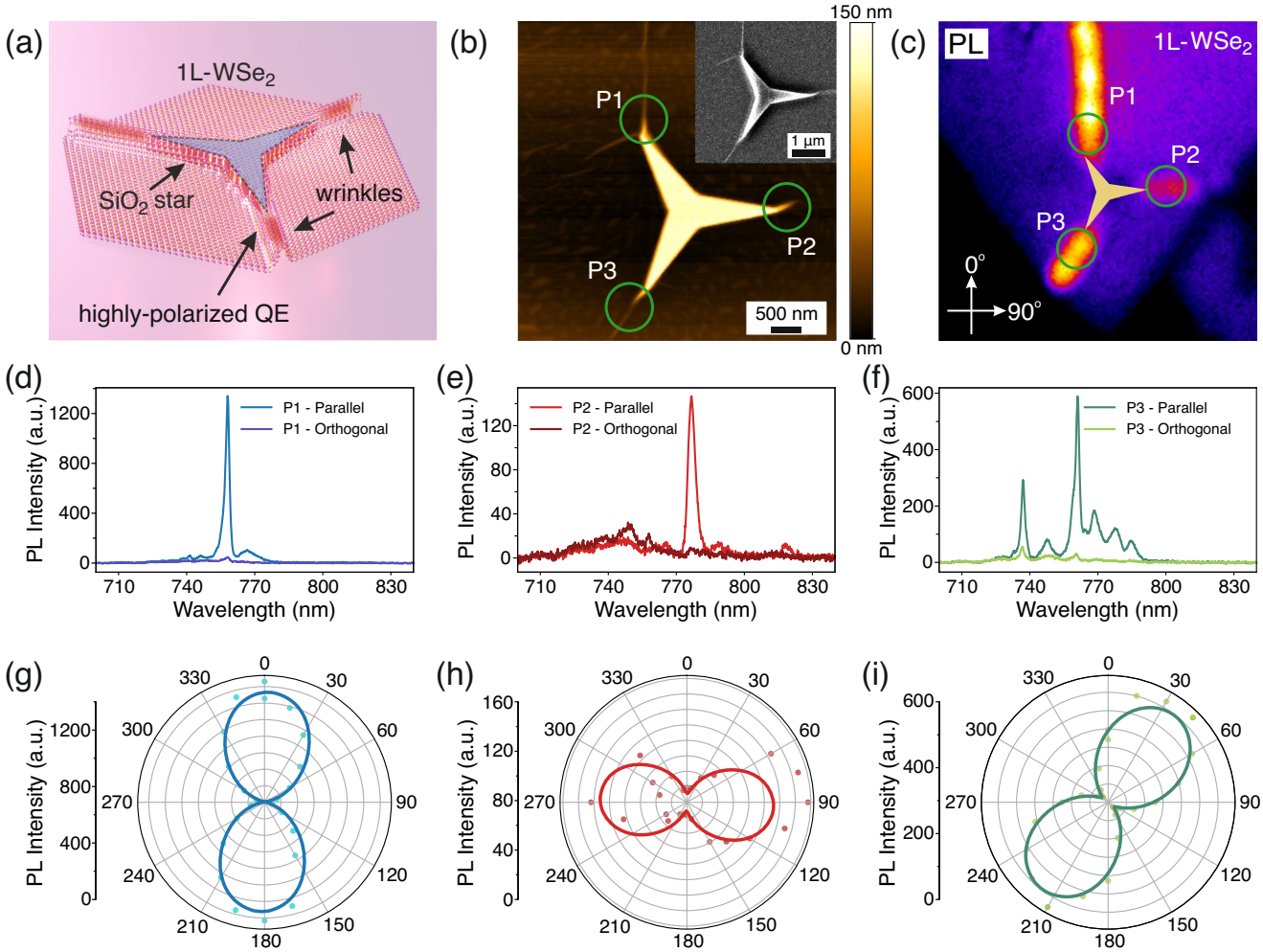

Fig. 2 | Highly polarized emission from WSe_2 quantum emitters with three-pointed star (TS) shaped pillars. a A sketch of monolayer-based WSe_2 quantum emitters with a star-shaped nanopillar design with a high aspect ratio. **b** AFM image of a WSe_2 monolayer flake deposited on the TS nanostructure depicted in (**a**). The inset in **b** shows the corresponding SEM image. Both images reveal the nanowrinkles forming along the vertices of the TS. The directionality of the formed nanowrinkles mostly follows the directions of the vertices. **c** Corresponding PL image taken at T = 4 K of the fabricated sample exhibits brighter localized emission signals along the nanowrinkles, in contrast to the planar region. The two orthogonal axes are given as a reference for the subsequent polarization-resolved spectra and polar plots. In both (**b**) and (**c**), the three collection regions (P1–3) are highlighted. **d**–**f** In-plane polarization-resolved PL spectra taken from three highlighted regions (P1–3), respectively. The presented PL spectra in (**d**–**f**) are measured under parallel and orthogonal in-plane polarization with respect to the direction of each nanowrinkle. **g**–**i** Corresponding polar plots of the polarization-resolved PL intensities for each peak, color-coded to match the graphs in (**d**–**f**). The solid lines represent sinusoidal fits[54] of the data, revealing a degree of linear polarization of 99 ± 4%, 82 ± 14%, and 93 ± 3%, respectively.

SPEs based on small cylindrical nanopillars emphasize the need for an effective strain-engineering approach to overcome these limitations.

Control of nanowrinkle orientation via novel nanopillar designs

We propose tailored nanostructure designs consisting of polygonal structures with long and sharp tips. As illustrated in Fig. 2a, their shape allows strain to be induced by the vertices, facilitating the creation of spatially isolated nanowrinkles. Commanding the directionality of the one-dimensional SPE-hosting nanowrinkles gives rise to an effective control of the polarization of the emitted single photons[18,25,31]. Here, we explore three different geometries, namely, a three-pointed star (TS), a five-pointed star (FS), and a bowtie (BT). The structures are patterned out of negative e-beam resist (HSQ), which is cured into SiO_2 upon e-beam exposure. The thickness of the nanostructures (~150 nm) was identified as optimal for producing nanowrinkles during the transfer process. Further details of the e-beam lithography and the remaining fabrication process are described in the "Methods" section.

First, we demonstrate WSe_2 single-photon emitters with a TS nanostructure. Figure 2a shows a 3D schematic representation of the TS nanostructure with a WSe_2 monolayer flake, illustrating the formation of nanowrinkles that follow the directionality of each arm. The surface morphology of a sample hosting a WSe_2 monolayer flake is shown in the atomic force microscope (AFM) image in Fig. 2b. The false coloring highlights the fabricated nanowrinkles versus the planar monolayer, with the inset providing a high-resolution SEM image of the same structure for clarity. We examine the morphological profiles of the fabricated nanowrinkles on the different designs in Supplementary Figs. 3–5. We notice clear similarities in the nanowrinkles between the different geometries, meaning that the flakes have a similar strain profile regardless of the design. More importantly, the nanowrinkles seem to be forming at the vertices, which was one of the primary reasons for tailoring these designs. Moreover, due to the size of the structures, the nanowrinkles are separated by more than 2 µm, allowing us to address each one individually. Nevertheless, the alignment between the arms and the nanowrinkles is imperfect and will be addressed in the following sections.

To investigate how these nanowrinkles modify the optical properties of monolayer WSe_2, we performed PL imaging under a 470 nm LED excitation in a closed-cycle optical cryostat equipped with a microscope objective (60×

, NA = 0.82) operating at T = 4 K. The obtained PL image (T = 4 K) taken from the TS sample is presented in Fig. 2c, where increased PL emission is observed along the nanowrinkles. On the contrary, the emission from the top of the TS structure, highlighted by a semi-transparent star, is comparable to that of the planar monolayer. According to the prevalent theoretical understanding, the mechanism behind the forming of SPEs in TMDs involves the interplay between local strain and defects. When local strain is applied to the monolayer with a sufficiently smooth profile, intervalley scattering remains negligible, allowing the modulation of the electronic bands and the efficient funneling of carriers to the higher-strained regions[11]. In these areas, the excitons are weakly localized while the effective mass of the carriers is reduced, enhancing charge mobility along the ridge of the nanowrinkle[36]. In the presence of defects, the strongly localized defect energy levels hybridize with the engineered bands. This hybridization breaks the valley locking and allows for the bright recombination of charge carriers at lower energetic levels within the band gap, resulting in novel emission lines. Previous theoretical studies indicate that the transition strength in these regions improves from 10^7 to 10^9 s^{-1}, leading to significantly increased photon emission[11]. The presented PL image in Fig. 2c verifies this theoretical claim, showing enhanced emission from areas where both defects and strain are present.

To gain some insights into the effect of the formed nanowrinkles on the polarization of the emitted photons, we performed the polarization-resolved μPL measurement by mounting a linear polarizer to the characterization setup presented in the "Methods" section. The collected PL spectra from the individual nanowrinkles (P1–P3) under parallel and orthogonal polarizations with respect to the directionality of each nanowrinkle are presented in Fig. 2d–f. All three emitters exhibit highly polarized emission, as the PL intensity of the orthogonal polarization is orders of magnitude lower than the parallel one. For further insight, we mapped the μPL spectra taken from the individual nanowrinkles as a function of the in-plane polarization, as shown in Fig. 2g–i, and noticed a highly linear polarized profile. To quantify the degree of linear polarization (DOLP) of the emitted photons, we use a sinusoidal fitting function and extract the DOLP using the maximum and minimum PL intensities as $(I_{max} - I_{min})/(I_{max} + I_{min})$, with the calculated values of 99 ± 4%, 82 ± 14%, and 93 ± 3%, respectively for the three emitters. The strong degree of linear polarization is attributed to the nanowrinkles, which give rise to a localized one-dimensional strain potential, thus forming strongly aligned dipoles[26,37]. Furthermore, the orientation of the linear polarization profiles appears to follow the directionality of the nanowrinkles. The AFM scans of the nanowrinkles presented in Supplementary Figs. 3–5 reveal proper height-to-base ratios, fulfilling the previously predicted condition[18] necessary for the dipole to align with the orientation of the nanowrinkle. Hence, the proposed design facilitates the successful fabrication of spatially isolated and highly linearly polarized SPEs in monolayer WSe_2. Despite the effective fabrication of SPEs, the TS structures produce nanowrinkles that are not perfectly aligned with their respective arms. With the purpose of reducing the extension of the nanowrinkles to create spatially confined emitters, we introduce the FS structure. We speculate that by increasing the number of vertices while maintaining the size of the structures, the nanowrinkles will shorten and be more localized around the tips.

In Fig. 3, we present similar data for investigating the proposed FS design. The AFM image in Fig. 3a showcases the surface morphology of the FS sample and the resulting nanowrinkles. Once more, the false coloring highlights the nanowrinkles, while the false-shading representation is shown in the inset for better contrast. Here, one of the five vertices has no visible nanowrinkle forming at its end. This is considered a normal occurrence due to the intricacies of the transfer process. Moreover, we observe that in the other four vertices (P1–P4), the nanowrinkles are indeed significantly shorter than those in the TS, leading to more localized SPEs. Despite this, the nanowrinkles are still well separated and can be addressed individually.

To further analyze the optical properties of the monolayer WSe_2 on the FS structure, we obtain the corresponding PL image (T = 4 K) under a 470 nm LED excitation, as shown in Fig. 3b. The PL signal significantly

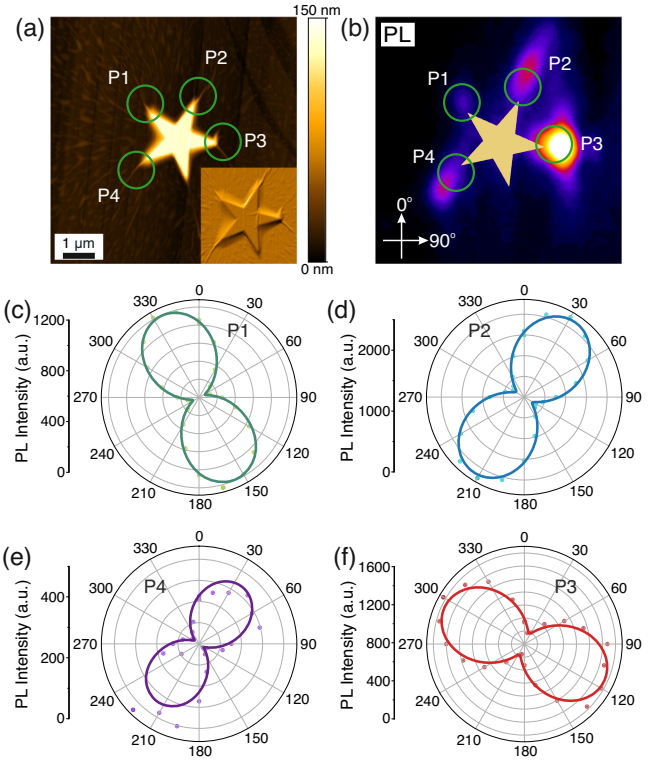

Fig. 3 | WSe_2 quantum emitters with a five-pointed star (FS) shaped pillars. **a** AFM image of a WSe_2 monolayer flake deposited on the FS nanostructure and false-shading representation (inset). Both the main image and the inset reveal nanowrinkles forming at the vertices, mostly following their directionality. **b** The corresponding PL image at T = 4 K reveals increased photon emission along the nanowrinkles. The two orthogonal axes are given as a reference for the upcoming polarization-resolved polar plots. Both **a** and **b** highlight the collection spots (P1–4) for the polarization-resolved polar plots to follow. **c–f** Corresponding polar plots of the polarization-resolved PL intensities collected from P1–4, fitted with a sinusoidal function. The calculated degree of linear polarization is 86 ± 2%, 81 ± 2%, 76 ± 3%, and 85 ± 11% for each peak respectively.

increases around the tips where the nanowrinkles are located (P1–P4), with the tip missing a nanowrinkle showing emission comparable to the pristine monolayer. To understand the effect of the nanowrinkles of the FS structure on the in-plane polarization of the single photons and compare it to that of the TS, we obtain polarization-resolved μPL spectra from the four highlighted spots. We extract the PL intensities and present them as polar plots in Fig. 3c–f. Similarly to Fig. 2, the sinusoidal fitting reveals that the emitted photons from each SPE demonstrate high DOLP, with the extracted values at 86 ± 2%, 81 ± 2%, 76 ± 3%, and 85 ± 11%, respectively. More importantly, the results reaffirm that the in-plane polarization's orientation follows the nanowrinkles' directionality, although our control over this directionality is still unsatisfactory. In general, the capability of the FS structure to host more localized and highly polarized emitters comes with the trade-off that certain vertices may not be able to form nanowrinkles.

While both the TS and FS structures demonstrate some promising amount of control over both the SPEs' localization and polarization, it is worth restating that the control of nanowrinkle directionality is not flawless. As shown in Figs. 2 and 3, possible misalignments between the arm and the nanowrinkle are possible. This behavior is attributed to the hexagonal lattice structure of the material and how its intrinsic "armchair" and "zigzag" directions[38] might affect the final directionality of the nanowrinkles. Moreover, a statistical analysis of the deviation in alignment between the directionality of the arms and the nanowrinkles of the TS and FS structures is presented in Supplementary Fig. 6. The Gaussian fitting of the analysis reveals a central position of 0.25° ± 2.55°. However, the standard deviation

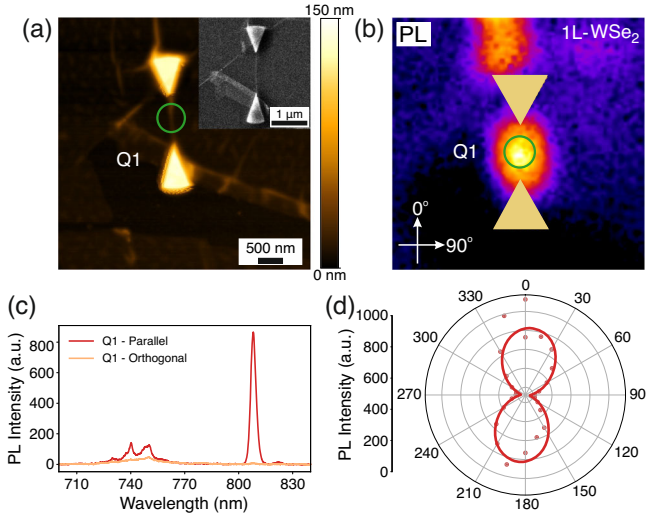

Fig. 4 | WSe_2 quantum emitters with bowtie (BT) shaped pillars. a AFM image of a WSe_2 monolayer flake deposited on a bowtie pair of triangular nanostructures. A single nanowrinkle connects the two structures and is visible both in the main image and in the SEM image of the corresponding inset. **b** The corresponding PL image, taken at T = 4 K, exhibits increased photon emission along the nanowrinkle connecting the triangles. The two orthogonal axes are given as a reference for the upcoming polarization-resolved spectrum and polar plot. Both **a** and **b** highlight the collection spot (Q1) for the characterized emitter. **c** The presented PL spectra are measured from emitter Q1 under parallel and orthogonal in-plane polarization with respect to the direction of the nanowrinkle, which coincides with the two orthogonal axes given in (**b**). **d** Corresponding polarization-resolved polar plot of the PL intensities from emitter Q1. The sinusoidal fitting reveals a degree of linear polarization of 92 ± 12%.

of 16.0° ± 2.5° highlights the demand for an improved design. Such BT structure is presented in Fig. 4. The BT design facilitates the formation of the nanowrinkle between the two triangles, localizing the emitters to the best of our ability. Additionally, any potential misalignment between the vertices and the nanowrinkle would be minimized while isolating the SPEs from any naturally forming deformation in the surrounding area. Figure 4a shows the AFM image of an exemplary BT structure with a monolayer WSe_2 flake. A nanowrinkle connecting the two triangles is clearly visible in both the AFM image and the SEM inset. Figure 4b presents the corresponding PL image of the structure, showing increased photon emission in the nanowrinkle (Q1). Furthermore, increased photon emission is also observed in the left corner of the top triangle, which is attributed to a nanowrinkle formed along the edge of the structure. Nevertheless, the separation between the two regions is sufficient to characterize them individually. Figure 4c presents the polarization-resolved μPL spectra, with the extracted intensities reported in the polar plot of Fig. 4d. Once again, the orientation of the in-plane polarization agrees with the directionality of the nanowrinkle, with an extracted DOLP of 92 ± 12%.

In addition, Supplementary Fig. 7 presents SEM images of four different exemplary BT structures, all hosting a nanowrinkle connecting the two triangles, with a bar graph illustrating the general trend of directionality. Most BT nanowrinkles are aligned along within ±2° from the desired orientation. In contrast to the TS and FS designs, the BT seems to address all the roadblocks, achieving better alignment of the nanowrinkle while sufficiently localizing the emitters and isolating them from the surrounding environment.

After examining all suggested designs, we have demonstrated BT structures that effectively control the in-plane polarization of the emitted single photons while dictating the spatial localization of the SPEs. To quantify the DOLP of the produced SPEs, we study the polarization profiles of 32 emitters and present them in Supplementary Fig. 8. The corresponding histogram is accompanied by a statistical analysis, with the fitted Gaussian distribution showing a central value of 0.84 and a standard deviation of 0.07. This value suggests that we indeed have highly linearly polarized single photons, indicating the effectiveness of our method.

Characterization of single-photon emission

In order to assess the quality of the fabricated SPEs based on the novel structures presented in this work, we proceed to the optical characterization of an exemplary WSe_2 nanowrinkle quantum emitter. For μPL measurements, we alter the excitation scheme from the CW LED to a 532 nm femtosecond pulsed laser (80 MHz) to optically excite the emitter. Supplementary Note 3 and Supplementary Fig. 9 present the reasoning for that change. Figure 5a shows a broad range (600–900 nm) μPL spectrum of an exemplary WSe_2 nanowrinkle emitter with a central wavelength of ~806.1 nm. A 750 nm long-pass filter was used to spectrally isolate the single-photon emission line from the delocalized exciton emission and excitation laser. The inset of Fig. 5a shows a high-resolution PL spectrum of the same emitter around its central wavelength, which exhibits a prominent zero-phonon line (ZPL) with a lower-energy phonon side band (PSB). The spectrum is fitted using a sum of a Lorentzian, representing the ZPL contribution (dashed red line), and a Gaussian, which captures the information related to the PSB contribution (dashed green line). We extract the linewidths of the two fitted curves, giving values of 0.35 ± 0.08 nm and 0.91 ± 0.04 nm, respectively, with the central wavelength of the PSB being red-detuned by 0.6 nm from the ZPL, resulting in an asymmetric PL emission spectrum. The increased contribution of the PSB to the total emission, evidenced by the ratio between the intensities ZPL:PSB = 49.2%:50.8%, suggests a strong exciton-phonon coupling for WSe_2 monolayer SPEs[39]. Even though the linewidth of the emission line is not Fourier-limited, being able to attain a narrow ZPL and resolve the PSB is attributed to the fabrication method that results in improved spatial isolation and a high linearly polarized emission.

To investigate the decay dynamics of the emitter, we perform the time-resolved PL (TRPL) measurement under the above-band pulsed excitation (Fig. 5b). Our data reveal two distinct decays, which are fitted with two separate exponential functions to extract the corresponding decay rates. The origin of the initial fast decay (τ_{fast} = 0.16 ± 0.24 ns) is not clear at this stage; however, it seems to come from a rapid process, limited by the instrument response function (IRF). A more detailed analysis is presented in Supplementary Note 4 and Supplementary Fig. 10. Nevertheless, despite its increased amplitude, the contribution of the fast decay accounts only for ~6% of the total curve. In contrast, the slow decay (τ_{slow} = 13.3 ± 0.2 ns) is the one that dominates the time-resolved response, making the largest contribution to the overall curve. Moreover, the calculated τ_{slow} is within the range of the reported lifetimes for localized SPEs in WSe_2 monolayer on dielectric substrates[13,16,18,20,37,40,41]. Finally, the abnormal increase in counts before the second decay begins may be caused by several factors. We attribute this rising behavior to trap states or excitation transfer processes that could lead to delayed decay and an initial rise in lifetime. Additionally, by potentially involving interactions with defects, non-radiative pathways may compete with the radiative decay, contributing to this rise.

While these complex decay dynamics require further investigation, their spectral stability is another critical aspect influencing the overall quality of SPEs. To study the stability of the emission signal from the fabricated WSe_2 nanowrinkle, we obtain the high-resolution time trace of the PL emission with an integration time of 0.2 s per frame under the same above-band laser excitation scheme (Fig. 5c). We observe wobbling of the emission line, which could be attributed to the unstable charge environment and noise due to photo-excited free carriers under the above-band excitation. As previously demonstrated[42], the encapsulation of the emitters using thin hBN flakes can stabilize the charge environment and minimize their spectral jittering. Nevertheless, this study focuses on bare WSe_2-based SPEs with no encapsulation or contact to stabilize the spectral fluctuations. For a qualitative analysis of this fluctuation, we perform a Gaussian fitting on

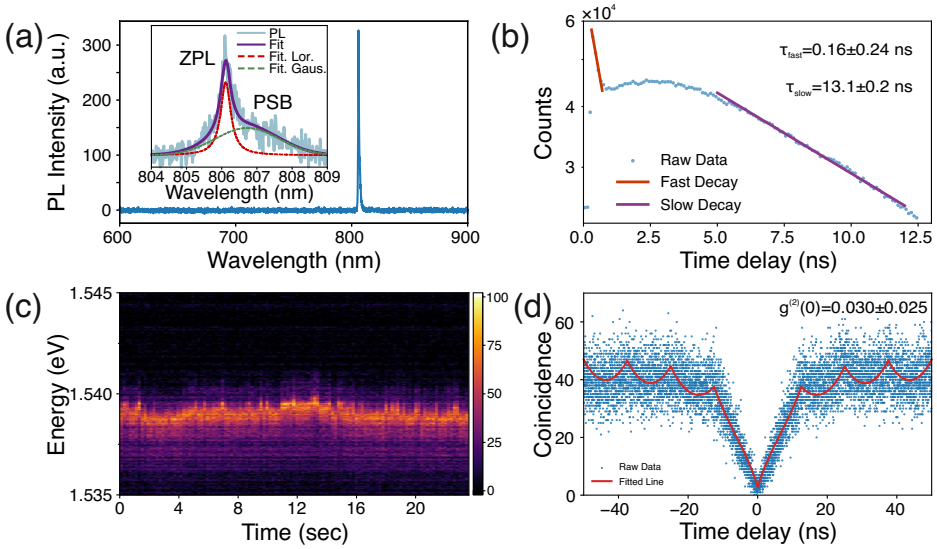

Fig. 5 | Single-photon characterization. a PL spectrum (4 K) taken from an exemplary single localized quantum emitter with high-degree polarization of 92 ± 12% under the above-band excitation of 532 nm femtosecond pulsed laser (80 MHz). The inset shows a high-resolution PL spectrum with a pronounced zero-phonon line (ZPL) and a low-energy broader phonon-side band. The fitting results exhibit the ZPL located at 806.1 nm, with a linewidth of 0.35 ± 0.08 nm. The broader PSB with a linewidth of 0.91 ± 0.04 nm is red-detuned by 0.6 nm to the ZPL, resulting in an asymmetric PL emission spectrum. **b** Semi-logarithmic plot of the lifetime measurement of the WSe_2 quantum emitter fitted with a biexponential function, resulting in a lifetime of $\tau_{fast} = 0.16 \pm 0.24$ ns and $\tau_{slow} = 13.3 \pm 0.2$ ns. **c** Time trace of PL emission signal, recorded using a high-resolution spectrometer with an integration time of 0.2 s per frame. The time trace data reveals a maximum wobbling span of approximately 1 meV for the ZPL. Fitting the distribution of the energy of the maxima for each line in the spectral map gives an average central position of the peak at 1.5365 eV with a standard deviation of 0.267 meV. **d** Corresponding second-order autocorrelation measurement ($g^{(2)}(\tau)$) of the emitter under the pulsed above band excitation, revealing an antibunching value of $g^{(2)}(0) = 0.030 \pm 0.025$.

the corresponding histogram presented in Supplementary Fig. 11, which reveals a fluctuation of the ZPL over ±0.5 meV around the mean central position of 1.5365 eV.

To evaluate the single-photon purity from the fabricated emitters, we performed the second-order correlation measurement under the aforementioned 80 MHz pulsed excitation using a typical HBT setup (Fig. 5d). The emission line from a representative nanowrinkle emitter was spectrally isolated by implementing a 750 nm long-pass filter. We observed peaks overlapping at non-zero delays, separated by the laser repetition time of 12.5 ns, resulting from the increased lifetime of the emitter. More importantly, the significantly low coincidence counts at zero time delay indicate the high purity of single-photon emission from the sample. To quantitatively assess single-photon purity, we employed a double-sided exponential function fitting for the adjacent peaks, yielding a value of $g^{(2)}(0) = 0.030 \pm 0.025$.

The results presented in the previous sections demonstrate the effectiveness of the method proposed in this study. Our novel approach reliably produces high-quality single-photon emitters characterized by both high single-photon purity and controlled polarization. Nevertheless, addressing the issues associated with previously discussed complicated dynamics and emission wobbling of our emitters is crucial for advancing photonic quantum information technology with TMD quantum emitters. These behaviors point to potential sources of additional inhomogeneous broadening, which can become the primary bottleneck for achieving lifetime-limited emission lines, resulting in poor indistinguishability. Therefore, turning our attention to identifying and dealing with possible inhomogeneous broadening could be the next step toward developing TMD-based quantum emitters with high purity and indistinguishability. Several strategies could be implemented to deal with such additional broadening.

On the one hand, it is essential to suppress the random charge fluctuations induced by free carriers on the substrate and the direct interaction of the emitters with the environment. One could implement a proper surface stabilization technique, such as encapsulation with Al_2O_3 via atomic layer deposition[43] or hBN encapsulation[12,44] which can be directly implemented to the method presented in this work. An alternative approach involves the implementation of electrical contacts[45,46]. On the other hand, an additional source of emission instability could result from the photo-induced charge carriers under the above-band optical excitation. One way to tackle this limitation lies in the employment of advanced excitation schemes, such as quasi-resonant[47], resonant[48,49], and SUPER excitation[50–52]. Implementing these schemes[47,48,50,51] in TMD quantum emitters can facilitate the efficient exciton population and the mitigation of additional exciton-phonon interactions.

In conclusion, we presented an efficient method for generating highly polarized single photons from orientation-controlled nanowrinkles in monolayer WSe_2. This method employs novel nanostructures to induce one-directional strain deterministically, enabling efficient control of the polarization of emitted single photons. We have successfully demonstrated single photon emission from WSe_2 nanowrinkle emitters with high purity ($g^{(2)}(0) = 0.030 \pm 0.025$) and a high degree of polarization (99 ± 4%). These findings provide crucial insights for the future integration of these quantum emitters into a specific mode of desired photonic structures, such as the TE mode of a planar ridge waveguide. Furthermore, understanding the fabrication limitations and critical aspects of deterministic polarization control of quantum emitters are essential steps toward their effective utilization as functional single-photon sources in quantum photonics.

Methods

Sample preparation

Nanopillar fabrication. We start with preparing the alignment marks (Ti (5 nm)/Au (50 nm)) on the thermally oxidized SiO_2 (110 nm)/Si substrate by a combination of UV-lithography and metal deposition, followed by the lift-off process. The role of the alignment marker is for further deterministic strain and defect engineering. The fabrication of the nanopillars was carried out by spin coating a high-resolution negative e-beam resist (hydrogen silsesquioxane or HSQ, XR-1541-006) at 3000 rpm for 1 min on the substrate with alignment markers, followed by two soft baking steps at 120 °C and 220 °C, both for 2 min. The resist was

patterned by an e-beam writer (JEOL 9500, 100 kV, 6 nA) with a dose of 11,000 μC/cm^2 and developed in a 1:3 solution of AZ 400K: H_2O to obtain 150 nm-tall nanopillars in four different shapes, namely cylindrical pillars, three-pointed stars, five-pointed stars, and bowties. It is worth remarking that a high dose is required to cure the spin-on dielectric, whose composition becomes SiO_2. Other negative e-beam resists with high sensitivity (activated at doses as low as 30 μC/cm^2) have also been tested (Supplementary Note 5 and Supplementary Fig. 12).

Exfoliation and transferring. WSe_2 flakes were first exfoliated from bulk crystals (HQ Graphene) via the scotch-tape method[53]. The flakes were then exfoliated on a polydimethylsiloxane (PDMS) stamp, which was prepared on a glass slide. The monolayers were identified by photoluminescence measurements using an optical microscope (Nikon 20× , NA = 0.45) and a 450 nm LED source. The transfer of the flakes to the nanostructures was performed under 70 °C using a transfer stage equipped with a heater and XYZ micropositioners. At this temperature, the van der Waals interactions between the flake and the substrate overcome the adhesion to PDMS, and the flake is released.

Defect fabrication. Defects were introduced on the monolayer lattice by bombarding the strained areas of the material with an e-beam (JEOL 9500 e-beam writer, 100 kV, 1000 μC/cm^2).

Optical characterization

Photoluminescence measurements. The PL measurements were obtained with a custom-built low-temperature micro-photoluminescence (μPL) setup. The sample is mounted on a closed-cycle cryostat (attoDRY800) operating at a base temperature of 4 K. The cryostat is equipped with piezoelectric nanopositioners and a low-temperature microscope objective (60× NA = 0.82) located inside the cryostat. The sample was excited with a CW LED at 470 nm for the PL imaging. For the micro-photoluminescence spectroscopy, a pulsed (80 MHz) femtosecond laser (Chameleon Ultra II, Coherent) at 532 nm was employed for the optical excitation of the emitters. Further investigation of the effect of the different excitation schemes on the emitters is presented in Supplementary Note 3 and Supplementary Fig. 9. The PL spectra were acquired with a fiber-coupled spectrometer (iHR 550, Horiba). A polarizer mounted on a motorized rotation mount was placed on the collection path for polarization-resolved measurements. PL images were acquired with an integration time of 1 s using a CMOS camera (Tucsen Dhyana, 4 MP).

Second-order correlation measurements. For second-order correlation measurements, we employed a fiber-optic Hanbury Brown and Twiss (HBT) interferometer. The photon counting was conducted using superconducting nanowires single-photon detectors (ID218, ID Quantique) connected to a time controller (ID900, IDQ).

Sample imaging

Bright-field (BF) images of the sample were taken using a confocal-microscopy setup equipped with an objective lens (Nikon LU Plan Fluor, 50× , NA = 0.8) and a CMOS camera (CS165MU/M, Thorlabs). The topographic images of the samples were obtained with a scanning electron microscope (SEM) (Zeiss Supra 40 VP, 5 kV, SE2 detector). To avoid creating further defects in the flakes, SEM imaging was carried out after all the measurements for optical characterization. Finally, the surface morphology of the samples, namely the width and height of the nanopillars and the WSe_2 nanowrinkles, was characterized by atomic force microscopy (Bruker Dimension Icon-PT, ScanAsyst-air tip).

Data availability

The data supporting the findings of this study are available within the main manuscript and its Supplementary Information files. Additional data are available from the corresponding authors upon reasonable request.

Received: 20 March 2024; Accepted: 29 August 2024;
Published online: 11 September 2024

References

1. Gregersen, N., McCutcheon, D. P. & Mørk, J. *Single-Photon Sources* 1st edn, Vol. 2, 585–604 (CRC Press, 2017).
2. Kwiat, P. G. et al. New high-intensity source of polarization-entangled photon pairs. *Phys. Rev. Lett.* **75**, 4337–4341 (1995).
3. Aharonovich, I., Englund, D. & Toth, M. Solid-state single-photon emitters. *Nat. Photonics* **10**, 631–641 (2016).
4. Heindel, T., Kim, J.-H., Gregersen, N., Rastelli, A. & Reitzenstein, S. Quantum dots for photonic quantum information technology. *Adv. Opt. Photonics* **15**, 613–738 (2023).
5. Tomm, N. et al. A bright and fast source of coherent single photons. *Nat. Nanotechnol.* **16**, 399–403 (2021).
6. Wang, H. et al. Towards optimal single-photon sources from polarized microcavities. *Nat. Photonics* **13**, 770–775 (2019).
7. Montblanch, A. R., Barbone, M., Aharonovich, I., Atatüre, M. & Ferrari, A. C. Layered materials as a platform for quantum technologies. *Nat. Nanotechnol.* **18**, 555–571 (2023).
8. Le, D. et al. Spin–orbit coupling in the band structure of monolayer WSe2. *J. Phys. Condens. Matter* **27**, 182201 (2015).
9. Gao, T., von Helversen, M., Antón-Solanas, C., Schneider, C. & Heindel, T. Atomically-thin single-photon sources for quantum communication. *npj 2D Mater. Appl.* **7**, 1–9 (2023).
10. Iff, O. et al. Strain-tunable single photon sources in WSe2 monolayers. *Nano Lett.* **19**, 6931–6936 (2019).
11. Linhart, L. et al. Localized intervalley defect excitons as single-photon emitters in WSe2. *Phys. Rev. Lett.* **123**, 146401 (2019).
12. Parto, K., Azzam, S. I., Banerjee, K. & Moody, G. Defect and strain engineering of monolayer WSe2 enables site-controlled single-photon emission up to 150 K. *Nat. Commun.* **12**, 3585 (2021).
13. Branny, A., Kumar, S., Proux, R. & Gerardot, B. D. Deterministic strain-induced arrays of quantum emitters in a two-dimensional semiconductor. *Nat. Commun.* **8**, 15053 (2017).
14. Xu, D. D. et al. Conversion of classical light emission from a nanoparticle-strained WSe2 monolayer into quantum light emission via electron beam irradiation. *Adv. Mater.* **35**, 2208066 (2023).
15. Wang, W., Jones, L. O., Chen, J.-S., Schatz, G. C. & Ma, X. Utilizing ultraviolet photons to generate single-photon emitters in semiconductor monolayers. *ACS Nano* **16**, 21240–21247 (2022).
16. Kumar, S., Kaczmarczyk, A. & Gerardot, B. D. Strain-induced spatial and spectral isolation of quantum emitters in mono- and bilayer WSe2. *Nano Lett.* **15**, 7567–7573 (2015).
17. Kern, J. et al. Nanoscale positioning of single-photon emitters in atomically thin WSe2. *Adv. Mater.* **28**, 7101–7105 (2016).
18. So, J. P. et al. Polarization control of deterministic single-photon emitters in monolayer WSe2. *Nano Lett.* **21**, 1546–1554 (2021).
19. Yu, L. et al. Site-controlled quantum emitters in monolayer MoSe2. *Nano Lett.* **21**, 2376–2381 (2021).
20. Iff, O. et al. Purcell-enhanced single photon source based on a deterministically placed WSe2 monolayer quantum dot in a circular Bragg grating cavity. *Nano Lett.* **21**, 4715–4720 (2021).
21. Palacios-Berraquero, C. et al. Large-scale quantum-emitter arrays in atomically thin semiconductors. *Nat. Commun.* **8**, 15093 (2017).
22. Kim, H., Moon, J. S., Noh, G., Lee, J. & Kim, J.-H. Position and frequency control of strain-induced quantum emitters in WSe2 monolayers. *Nano Lett.* **19**, 7534–7539 (2019).
23. Zhao, H., Pettes, M. T., Zheng, Y. & Htoon, H. Site-controlled telecom-wavelength single-photon emitters in atomically-thin MoTe2. *Nat. Commun.* **12**, 6753 (2021).
24. Luo, Y. et al. Deterministic coupling of site-controlled quantum emitters in monolayer WSe2 to plasmonic nanocavities. *Nat. Nanotechnol.* **13**, 1137–1142 (2018).

25. Azzam, S. I., Parto, K. & Moody, G. Purcell enhancement and polarization control of single-photon emitters in monolayer WSe2 using dielectric nanoantennas. *Nanophotonics* **12**, 477–484 (2023).
26. Drawer, J. C. et al. Monolayer-based single-photon source in a liquid-helium-free open cavity featuring 65% brightness and quantum coherence. *Nano Lett.* **23**, 8683–8689 (2023).
27. Schuler, B. et al. Electrically driven photon emission from individual atomic defects in monolayer WS2. *Sci. Adv.* **6**, eabb5988 (2020).
28. Lenferink, E. J. et al. Tunable emission from localized excitons deterministically positioned in monolayer p–n junctions. *ACS Photonics* **9**, 3067–3074 (2022).
29. Zhang, D., Zhai, D., Deng, S., Yao, W. & Zhu, Q. Single photon emitters with polarization and orbital angular momentum locking in monolayer semiconductors. *Nano Lett.* **23**, 3851–3857 (2023).
30. Ma, Y. et al. On-chip spin-orbit locking of quantum emitters in 2d materials for chiral emission. *Optica* **9**, 953–958 (2022).
31. Wang, Q. et al. Highly polarized single photons from strain-induced quasi-1d localized excitons in WSe2. *Nano Lett.* **21**, 7175–7182 (2021).
32. Wang, J., Sciarrino, F., Laing, A. & Thompson, M. G. Integrated photonic quantum technologies. *Nat. Photonics* **14**, 273–284 (2020).
33. Dang, J. et al. Identifying defect-related quantum emitters in monolayer WSe2. *npj 2D Mater. Appl.* **4**, 2 (2020).
34. Iff, O. et al. Deterministic coupling of quantum emitters in WSe 2 monolayers to plasmonic nanocavities. *Opt. Express* **26**, 25944–25951 (2018).
35. Errando-Herranz, C. et al. Resonance fluorescence from waveguide-coupled, strain-localized, two-dimensional quantum emitters. *ACS Photonics* **8**, 1069–1076 (2021).
36. Velja, S., Krumland, J. & Cocchi, C. Electronic properties of MoSe2 nanowrinkles. *Nanoscale* **16**, 7134–7144 (2024).
37. Tripathi, L. N. et al. Spontaneous emission enhancement in strain-induced WSe2 monolayer-based quantum light sources on metallic surfaces. *ACS photonics* **5**, 1919–1926 (2018).
38. Le, D. & Rahman, T. S. Joined edges in MoS2: metallic and half-metallic wires. *J. Phys. Condens. Matter* **25**, 312201 (2013).
39. Mitryakhin, V. N. et al. Engineering the impact of phonon dephasing on the coherence of a WSe2 single-photon source via cavity quantum electrodynamics. *Phys. Rev. Lett.* **132**, 206903 (2024).
40. He, Y.-M. et al. Single quantum emitters in monolayer semiconductors. *Nat. Nanotechnol.* **10**, 497–502 (2015).
41. Srivastava, A. et al. Optically active quantum dots in monolayer WSe2. *Nat. Nanotechnol.* **10**, 491–496 (2015).
42. Daveau, R. S. et al. Spectral and spatial isolation of single tungsten diselenide quantum emitters using hexagonal boron nitride wrinkles. *APL Photonics* **5**, 096105 (2020).
43. Kim, S. Y., Park, S. & Choi, W. Enhanced carrier mobility of multilayer MoS2 thin-film transistors by Al_2O_3 encapsulation. *Appl. Phys. Lett.* **109**, 152101 (2016).
44. Kutrowska-Girzycka, J. et al. Exploring the effect of dielectric screening on neutral and charged-exciton properties in monolayer and bilayer MoTe2. *Appl. Phys. Rev.* **9**, 041410 (2022).
45. Schadler, K. G. et al. Electrical control of lifetime-limited quantum emitters using 2d materials. *Nano Lett.* **19**, 3789–3795 (2019).
46. Zhai, L. et al. Low-noise GaAs quantum dots for quantum photonics. *Nat. Commun.* **11**, 4745 (2020).
47. Bao, D. et al. Probing momentum-indirect excitons by near-resonance photoluminescence excitation spectroscopy in WS2 monolayer. *2D Mater.* **7**, 031002 (2020).
48. Kumar, S. et al. Resonant laser spectroscopy of localized excitons in monolayer WSe 2. *Optica* **3**, 882–886 (2016).
49. Somaschi, N. et al. Near-optimal single-photon sources in the solid state. *Nat. Photonics* **10**, 340–345 (2016).
50. Bracht, T. K. et al. Swing-up of quantum emitter population using detuned pulses. *PRX Quantum* **2**, 040354 (2021).
51. Karli, Y. et al. SUPER scheme in action: experimental demonstration of red-detuned excitation of a quantum emitter. *Nano Lett.* **22**, 6567–6572 (2022).
52. Vannucci, L. et al. Single-photon emitters in WSe2: critical role of phonons on excitation schemes and indistinguishability. *Phys. Rev. B* **109**, 245304 (2024).
53. Castellanos-Gomez, A. et al. Deterministic transfer of two-dimensional materials by all-dry viscoelastic stamping. *2D Mater.* **1**, 011002 (2014).
54. Koudinov, A., Akimov, I., Kusrayev, Y. G. & Henneberger, F. Optical and magnetic anisotropies of the hole states in Stranski-Krastanov quantum dots. *Phys. Rev. B* **70**, 241305 (2004).

Acknowledgements

The authors acknowledge support from the European Research Council (ERC-StG "TuneTMD", grant no. 101076437) and the Villum Fonden (grant no. VIL53033). The authors also acknowledge the European Research Council (ERC-CoG "Unity", grant no. 865230), and Carlsberg Foundation (grant no. CF21-0496). Last but not least, the authors acknowledge the cleanroom facilities at DTU Nanolab—National Centre for Nano Fabrication and Characterization.

Author contributions

A.P. fabricated the quantum emitter samples. C.P. and A.M. supported the project by fabricating various shaped pillars for strain engineering. A.P., C.P., A.M., and B.M. performed optical measurements from the fabricated samples. A.P., P.M., and C.P. contributed to data analysis and processing. B.M. conceived the idea, and L.V., N.G., and B.M. coordinated the project. A.P., P.M., and B.M. wrote the manuscript with input from all co-authors.

Competing interests

The authors declare no competing interests.

Additional information

Supplementary information The online version contains supplementary material available at https://doi.org/10.1038/s41699-024-00497-2.

Correspondence and requests for materials should be addressed to Battulga Munkhbat.